Rock and Soil Mechanics

Volume 44 | Issue 4 Article 8

7-19-2023

Numerical study on seismic behavior of shield tunnel crossing saturated sandy strata with different densities

Hong WU
School of Civil and Hydraulic Engineering, Huazhong University of Science and Technology, Wuhan, Hubei 430074, China

Zhi YE
School of Civil and Hydraulic Engineering, Huazhong University of Science and Technology, Wuhan, Hubei 430074, China

Yu-ting ZHANG
Geotechnical Engineering Research Center, Tianjin Research Institute for Water Transport Engineering of Ministry of Transport, Tianjin 300456, China

Hua-bei LIU
School of Civil and Hydraulic Engineering, Huazhong University of Science and Technology, Wuhan, Hubei 430074, China

Follow this and additional works at: https://rocksoilmech.researchcommons.org/journal

 Part of the Geotechnical Engineering Commons

Recommended Citation

WU, Hong; YE, Zhi; ZHANG, Yu-ting; and LIU, Hua-bei (2023) "Numerical study on seismic behavior of shield tunnel crossing saturated sandy strata with different densities," *Rock and Soil Mechanics*: Vol. 44: Iss. 4, Article 8.
DOI: 10.16285/j.rsm.2022.5741
Available at: https://rocksoilmech.researchcommons.org/journal/vol44/iss4/8

This Article is brought to you for free and open access by Rock and Soil Mechanics. It has been accepted for inclusion in Rock and Soil Mechanics by an authorized editor of Rock and Soil Mechanics.

Rock and Soil Mechanics 2023 44(4): 1204−1216 ISSN 1000−7598
https: //doi.org/10.16285/j.rsm.2022.5741 http://rocksoilmech.researchcommons.org/journal

Numerical study on seismic behavior of shield tunnel crossing saturated sandy strata with different densities

WU Hong[1], YE Zhi[1], ZHANG Yu-ting[2], LIU Hua-bei[1]

1. School of Civil and Hydraulic Engineering, Huazhong University of Science and Technology, Wuhan, Hubei 430074, China
2. Geotechnical Engineering Research Center, Tianjin Research Institute for Water Transport Engineering of Ministry of Transport, Tianjin 300456, China

Abstract: Earthquake-induced liquefaction poses a significant threat to underground structures. Particularly, tunnel structures located at the interface of different liquefaction-resistant strata are more prone to severe seismic damages. In this paper, a three-dimensional numerical study was carried out to investigate the seismic response of a shield tunnel passing through saturated sandy strata with different densities. Firstly, a boundary interface model that describes the liquefaction behavior of sand with different densities was used to simulate saturated sand, which was validated by shaking table experiments on a tunnel embedded in liquefiable soil. Secondly, a multi-degree-of-freedom link spring is applied to characterize the interaction between segment rings. The approach was validated using the stepwise loading experimental results of assembled segment rings in Refs. [35] and [37]. Finally, a 3D numerical model of shield tunnels crossing two different densities saturated sand strata was established to study the effects of relative densities of soil, peak input accelerations, and the dip angle of the interface on the dynamic response of sand stratum-tunnel system. The results indicate that horizontal displacements of the tunnel under seismic excitations are coupled with the excess pore pressure induced by vertical uplifts, and deformation of the tunnel is not simultaneous in the two soil strata, resulting in twisting distortion of the tunnel structure. The uplifts of the tunnel change rapidly and are increased with increasing dip angle near the soil interface. Also, bending moments suddenly change, and shearing/tensile displacements of joints increase remarkably, which confirms that the seismic design of underground structure segments near the soil interface is a critical issue.

Keywords: saturated soil interface; shield tunnel; earthquake responses; deformation mode; soil liquefaction

1 Introduction

With the increasing number of cross-river/sea tunnels in China, the seismic performance of shield tunnel structures in complex and water-rich strata has attracted much attention. Loose soil and fine sandy strata are potentially susceptible to liquefaction during earthquakes. In past seismic disasters, many underground structures have suffered varying degrees of serious damage such as liquefaction-induced uplift, uneven settlement, shear failure, and joint water inflow[1−3]. As long underground structures, tunnels inevitably pass through saturated soil layers with different liquefaction risks. Therefore, the seismic response characteristics of tunnel structure segments at the intersection of these strata are one of the key scientific issues that urgently need to be studied.

The longitudinal non-uniformity of soil significantly affects the dynamic response characteristics of tunnel structures. Many scholars have explored this issue through theoretical analysis[4−5], model tests[6−10], and numerical simulations. Although the model tunnel structures and soil properties varied in each study, there was a sudden change in strain and acceleration responses at the intersection of different strata, with stress concentration phenomena, indicating that tunnel structures at the intersections among strata are prone to earthquake damage. However, most studies did not consider the effect of groundwater. In fact, for cross-river/sea tunnels in water-rich strata, the potential liquefaction risk under earthquakes cannot be ignored. Existing studies[11−15] demonstrate that the accumulation law of excess pore water pressure under seismic action on liquefiable sites will significantly affect the mechanical response and deformation law of underground structures. This also indicates that the response mechanism of underground structures at the intersections among liquefiable soil formations will be more complex.

There is currently a lack of numerical simulation studies on the aforementioned issue. Compared to model experiments, reasonable numerical simulation studies not only require less investment, but also allow for a more detailed examination of the dynamic interaction between underground structures and saturated soil under seismicity. Therefore, numerical simulation studies are a critical supplement to model experiment research and an important

Received: 18 May 2022 Accepted: 8 September 2022
This work was supported by the National Natural Science Foundation of China (NSFC) (51978305) and the Fundamental Research Funds for the Central Public Welfare Research Institutes (TKS20220107).
First author: WU Hong, male, born in 1993, PhD candidate, research interests: aseismic research on underground structures. E-mail: wuhong.phd@gmail.com
Corresponding author: LIU Hua-bei, male, born in 1973, PhD, Professor, research interest: geosynthetic reinforcement technology and seismic analysis of geotechnical structures. E-mail: hbliu@hust.edu.cn

means of studying the response mechanism of underground structures at the interface of liquefiable soil layers. The primary issue to be addressed in numerical simulation analysis is how to describe the dynamic fluid-solid coupling response characteristics of saturated sand layers. As a result, many elastoplastic cyclic constitutive models have been developed, including a representative unified boundary interface model for sand based on critical state theory[16−19]. This type of models can uniformly describe the coupling changes in effective stress and pore water pressure of saturated sand layers under different confining pressures and compactions during dynamic loading process, allowing for liquefaction or incomplete liquefaction analysis. The capabilities of each model have been verified and fully discussed in multiple centrifuge shaking table tests. Among them, Chen[20] used the CycLiqCPSP model[21] to study the dynamic response of underground structures crossing locally liquefiable layers longitudinally. The results showed that the shear force and additional bending moment at the structure segment at the layer interface significantly increased, and that there were significant differences in structural response with varying length and thickness of liquefiable zones.

It is also crucial to rationalize modeling for shield tunnel structures in numerical models. Considering time costs, overly refined modeling methods should not be used for long shield tunnel models[22], but rather simplified models should be adopted for structures. Chen et al.[23] and Miao et al.[24] used beam elements and spring elements to establish a simplified soil−tunnel structure model for numerical analysis in ABAQUS, focusing on the joint bolt tension and seam opening. Liao et al.[25] and Wu et al.[26] pointed out that the shear effect between tunnel rings cannot be ignored when longitudinal non-uniform deformation occurs. Do et al.[27−28] proposed a simplified simulation method that can simultaneously consider joint bolt shear and tension as well as rotational deformation, using multi-degree-of-freedom connecting springs to characterize the interaction between ring joints, which has been applied in FLAC^{3D}.

Regarding the seismic response of shield tunnels crossing saturated sand layers with different relative densities, this paper firstly briefly introduces the proposed soil boundary model and validates it. Secondly, a simulation method for long-span shield tunnels that considers the interaction between segment joints is presented, which can effectively characterize the force and deformation characteristics of segment joints under dynamic loads, and its feasibility is verified. Finally, a three-dimensional numerical analysis model is established to study the dynamic fluid-solid coupling response characteristics of the strata−tunnel system with different relative densities. The factors such as input seismic amplitude, relative density of adjacent sand layers, and intersection inclination angle are analyzed to summarize the seismic response laws of tunnels.

2 Numerical simulation methods and validation

2.1 Constitutive model and validation

In this paper, the saturated sandy soil is modeled using the P2PSand model[29], a built-in practical two-surface plastic sand constitutive model in FLAC^{3D} 7.0. This model incorporates the relative density variable into control equations within the theoretical framework of the unified boundary surface model DM04[16], and further optimizes it. The P2PSand model corrects the plastic shear modulus under repeated loadings to solve the problems of (1) no increase in shear strain during cyclic loadings, and (2) excessive hysteresis loops at large shear strains. This enables the P2PSand model to better characterize the cyclic flow characteristics of saturated sandy soils and can be used to study the dynamic response characteristics of sandy soil layers with different relative densities during earthquakes. The model has been used to validate monotonic or cyclic laboratory tests[19] and centrifuge tests[30] on sandy soils, achieving satisfactory results.

In the subsequent analysis, the saturated soil layers are assumed to be Toyoura sand. The corresponding P2PSand model parameters are obtained from Ref.[19], based on static and dynamic unit tests, as listed in Table 1. To further verify the rationality of the constitutive model and its parameters, a FLAC^{3D} numerical model is established to simulate the shaking table test of underground structures in Ref.[31]. In this test, the soil layer is saturated Toyoura sand with similar specifications. Since the laboratory test results of the experimental sand are not provided in Ref.[31], its model parameters are from Ref.[19], as shown in Table 1. The schematic of "Model F" shaking table test in Ref.[31] is shown in Fig. 1, where a PMMA square box with an apparent weight of 8 kN /m^3 was buried in a sand layer with a relative density of 42%. An 8 cm thick compacted Toyoura sand layer was laid at the bottom of the model box and saturated with water. A 4-second sine wave with an amplitude of 2.7g at a frequency of 5 Hz was applied on the bottom of the model. The pore pressure P_{M2} located in the soil beneath the box, the pore pressures P_3 and P_{13} lied directly on the side of P_{M2}, and the vertical displacement D_{M3} at the top of the box were monitored. Shell elements were used to simulate underground structures in numerical models. Since contact strength information between tunnel models and saturated soils was not provided in Ref.[31], soil−structure contact surfaces were not analyzed deeply

https://rocksoilmech.researchcommons.org/journal/vol44/iss4/8
DOI: 10.16285/j.rsm.2022.5741

in this study. The rigid connection method between shell elements and soil was used by default, assuming that contact between soil and structure remains intact throughout without detachment during calculations.

Table 1 Parameters of P2Psand model for Toyoura sand

Elasticity parameters		Friction angle at critical state	Maximum void ratio	Minimum void ratio	Critical state parameters			Factor of cycling	Factor of elasticity degradation
g_0	C_{dr}	φ_{cs}/(°)	e_{max}	e_{min}	D_{rc0}	λ_c	ξ	K_c	K_d
180	1.15	31.6	0.977	0.597	0.115	0.05	0.7	$K_c = 0.63-0.25D_{r0}$	$K_d = 0.41-0.167D_{r0}$

Note: D_{r0} represents the initial relative density of sandy soils.

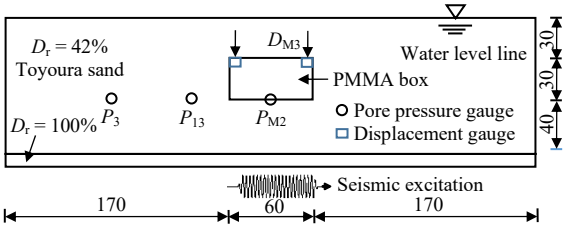

Fig. 1 Cross-section of the model test F in a shaking table test (unit: cm)

The comparison results are shown in Fig. 2. It should be noted that due to the inability to accurately obtain the fluctuation time history of the experimental excess pore pressure, the envelope curves (dashed lines) of fluctuation curves of pore pressure were selected for comparison. The numerical simulation can basically reproduce the experimental results well. At the beginning of seismic excitation, the fluctuation of simulated pore pressure is larger and negative pore pressure can be observed. The reason for this may be that sand properties of the P2PSand model are confining pressure-dependent, and unstable pore pressure may occur under low confining pressures on a 1*g* shaking table. In other words, the model's prediction of pore pressure in low confining pressure sandy soil layers with a surface layer of 1−2 meters fluctuates greatly. However, for the tunnel buried at a depth of 7.5 m in this paper, the dynamic response of the tunnel structure and adjacent soil layers that are of primary concern are not significantly affected. In addition, the simulated final uplift of the tunnel is slightly smaller, which may be due to less friction between the tunnel model and saturated soil.

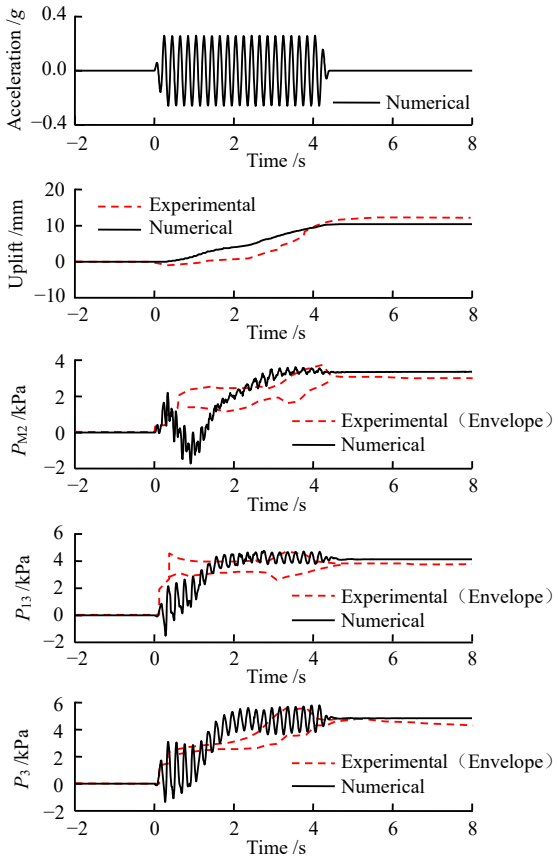

Fig. 2 Comparisons of tunnel uplift and pore pressure development from numerical and experimental results

2.2 Simulation and validation of segment joints

Based on the research of Do et al.[27−28], this paper presents a three-dimensional "ring-link-ring" simulation method for long shield tunnel structures. This method uses shell elements to simulate the segmental structure of the shield tunnel, but simplifies the contacts between concrete surfaces at joints as discrete point contacts, which are treated differently with the connection bolts corresponding to link connection springs, allowing for independent consideration of their contributions to joint performance. Figure 3 shows the schematic diagram of segments and bolt connection. The connection spring corresponding to the 16 bolts between rings is represented by B-link (joints at the bolt position), while the face contacts between adjacent segment rings are simulated by discrete point contact springs, i.e., C-link (joints at the concrete segments) at the non-bolt position. The number of C-links should not be excessive, as it increases computational cost, nor too few, as it should meet the minimum mesh size requirements for dynamic calculations. Based on actual longitudinal bolt numbers in shield tunnels, this paper suggests that the number of C-links be three times that of B-links, which is discussed further in the model

validation section at the end of this section.

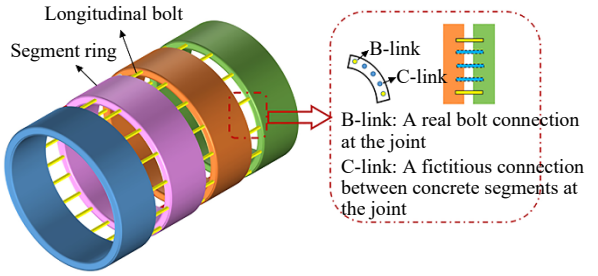

Fig. 3 Diagram of connections between tunnel segments and bolts

Deformation modes of normal, shear, bending, and torsion can be defined for both B-link and C-link. The stress−strain relationships of these links can be determined by material properties, such as the compression/tension stiffness (EA), shear stiffness (GA), bending stiffness (EI), and torsional stiffness (GI_p) of the cross-section. Alternatively, they can be determined based on relevant model test results and engineering practice experience and assigned to the links. Assuming that each link acts independently without considering the coupling relationship among them, the radial (z-direction) and tangential (x-direction) shear stiffnesses are equal and linear. Meanwhile, the contribution of C-link is ignored in the rotational degree of freedom. Figures 4 and 5 show schematic diagrams of spring connections at one B-link and two C-links at an Inter-ring joint in various degrees of freedom, which are taken as an example to state the method for setting joint parameters in detail.

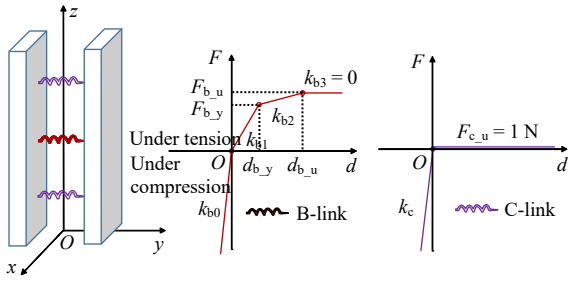

Fig. 4 Springs of joints in the normal direction

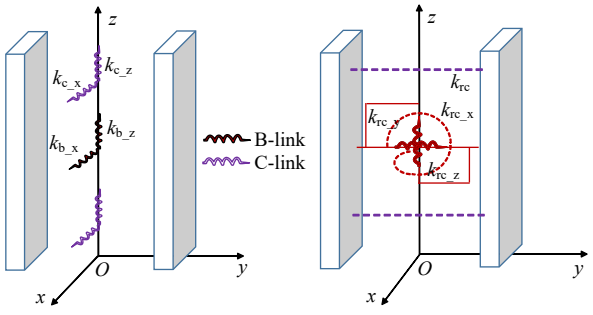

(a) Tangential springs (b) Rotational springs

Fig. 5 Springs of joints in both tangential and rotational directions

The relationship between the force and displacement of the C-link and B-link in the normal (y) direction exhibits a multi-segmented line form. As shown in Fig. 4, when the joint is under compression, the average compression stiffness k_c of the concrete in the joint is assigned to the C-link, while the equivalent compression stiffness of the B-link is the sum of k_c and the compression stiffness of single bolt. When the joint is under tension, a minimal tensile yield strength is applied to C-link to ensure that it can only withstand the compressive force but not the tensile force, while B-link is set as a bilinear yield spring when subjected to tension with its parameters determined by the tensile properties of the corresponding bolt. The spring parameters k_{c_y} and k_{b_y} for C-link and B-link in the normal direction are

$$k_{c\_y}=\begin{cases}k_c=E_cA_c/(l_c\,n) & (d\leqslant 0)\\ 0 & (d>0)\end{cases} \tag{1}$$

$$k_{b\_y}=\begin{cases}k_{b0}=E_bA_b/l_b+k_c & (d\leqslant 0)\\ k_{b1}=E_bA_b/l_b & (0<d\leqslant d_{b\_y})\\ k_{b2}=0.01\,k_{b1} & (d_{b\_y}<d\leqslant d_{b\_u})\\ 0 & (d>d_{b\_u})\end{cases} \tag{2}$$

where k_c represents the average compression stiffness of C-links; k_{b0} is the equivalent compression stiffness of B-links; k_{b1} and k_{b2} denote the initial tension stiffness and the post-yield tension stiffness respectively; the values of d_{b_y} and d_{b_u} represent the yielding displacement and ultimate displacement of bolts under tension, which can be calculated based on bolt length and stress−strain relationship; E_cA_c and E_bA_b represent the tension and compression stiffnesses of cross-sections of concrete and single bolt, respectively; l_b and l_c denote bolt length and segment thickness, respectively; and n represents the total number of links.

For B-link in the shear direction, its parameters are determined based on the shear stiffness of the bolt section (as shown in the following two equations). Considering the reduction of stiffness caused by clearance between the bolt and sleeve, the free length x_b of the shear segment of the bolt is taken as the bolt length in this study. For C-link, it is difficult to comprehensively consider factors such as friction coefficient between contact surfaces of segments, rubber pads, and mortise and tenon connection structures. According to relevant research results[32−34], the empirical value of shear stiffness for inter-ring joints is 50−400 MN /m along the arc direction. When C-link is disengaged in the normal direction (d_c>0), its tangential shear stiffness is set to 0.

$$k_{b\_x}=k_{b\_z}=G_bA_b/x_b \tag{3}$$

$$k_{c\_x}=k_{c\_z}=\begin{cases}K_{ref}\times C/n_c & (d_c\leqslant 0)\\ 0 & (d_c>0)\end{cases} \tag{4}$$

where k_{b_x}, k_{b_z}, k_{c_x} and k_{c_z} are shear stiffness along the x and z directions; G_bA_b is the shear stiffness of the cross-section; x_b is the free length of the shear section of the bolt, which is the bolt length herein; n_c is the total number of C-links; C is the average circumference of the circular segment section; K_{ref} is the reference value for joint shear stiffness per meter along the arc length. In this study, K_{ref} is 122 MN /m, as detailed in Section 3.2.

$$\left.\begin{aligned}&k_{br\_x}=E_bI_x\ ,\ k_{br\_z}=E_bI_z\ ;\ k_{br\_y}=G_bI_p\\ &k_{cr\_x}=k_{cr\_y}=k_{cr\_z}\ :\ \text{Free}\end{aligned}\right\} \tag{5}$$

As shown in Fig. 5 and Eq. (5), for the B-link, let the section flexural stiffnesses k_{br_x} and k_{br_z} corresponding to the bending moments M_{b_x} and M_{b_z} be equal, which are determined by the section flexural stiffness E_bI_b of the corresponding bolts. Meanwhile, the section torsional stiffness k_{br_y} corresponding to the torque T_{b_y} is the torsional stiffness G_bI_p of a circular shaft. For C-links, assuming that the rotational behavior of the nodes on the contact surface of the segment is free, i.e., setting all the rotational stiffness k_{cr_x}, k_{cr_x} and k_{cr_x} of C-link to be a free state.

Using the proposed simulation method for segment joints, the monotonic loading tests of homogeneous seamless and seamed segment ring models in Ref.[35] were validated. In the experiment, the segment rings were made of organic glass with an outer diameter, thickness, and ring width of 0.4 m, 0.023 m, and 0.065 m, respectively. The elastic modulus and Poisson's ratio were 2.06 GPa and 0.3, respectively. The bolts were made of aluminum welding wire with a diameter, length, and quantity of 0.002 m, 0.027 m, and 6, respectively, and its elastic modulus and Poisson's ratio were 33.8 GPa and 0.32, respectively. Figure 6 illustrates the loading model schematic diagram with simply supported structure at both ends, applying nine levels of loads on the 9th and 17th rings, recording displacements after each level of loads was balanced. Shell elements were used to simulate the segment rings in the numerical model. Homogeneous circular pipes were simulated using shell elements without joints while assembled segment rings were simulated using the new proposed method. Six B-links in the model represented bolt connections while C-links were set to be 10, 18, 26, 48 to study their influence on results. Since the surface of plexiglass was relatively smooth, C-links were assumed to be free tangentially with specific parameter values listed in Set A in Table 2.

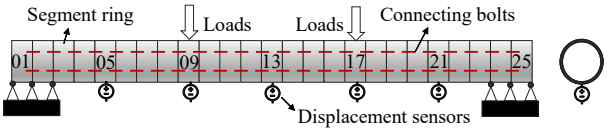

Fig. 6 Segmental models under longitudinal loading[35]

Table 2 Parameters of B-link and C-link springs

Connection properties		Normal direction					Shear direction		Rotation direction	
		Compression stiffness /(MN • m^{-1})	Initial tensile stiffness /(MN • m^{-1})	post-yield tensile stiffness /(MN • m^{-1})	Yield tension /MN	Limit tension /MN	Radial shear stiffness /(MN • m^{-1})	Tangential shear stiffness /(MN • m^{-1})	Bending spring stiffness /(kN • m • rad^{-1})	Torsion spring stiffness /(kN • m • rad^{-1})
Set A	B-link	30.93	3.93	0.039 3	6.3×10^{-4}	6.9×10^{-4}	5.960	5.960	2.65×10^{-5}	2.01×10^{-5}
	C-link	27.00	—	—	—	1×10^{-6}	Free	Free	Free	Free
Set B	B-link	1.30	0.20	0.002 0	9×10^{-4}	1.05×10^{-3}	0.077	0.077	1.27×10^{-5}	0.98×10^{-5}
	C-link	1.10	—	—	—	1×10^{-6}	Free	Free	Free	Free
Set C	B-link	2 944.00	364.00	3.640 0	0.452	0.566	140.000	140.000	8.19	6.30
	C-link	2 580.00	—	—	—	1×10^{-6}	46.700	46.700	Free	Free

To verify the validity of discretizing the surface contacts of concrete into point contacts, this paper also presents a more refined numerical model for comparison, which used solid elements to simulate the assembled tunnel segment structure, and assumed a relatively smooth surface for the organic glass at the inter-ring contact surface, with a friction angle and cohesion of 17º and 0.1 kPa, respectively, based on the results in Ref.[36]. The normal stiffness and tangential stiffness were set to 423.6 GPa /m according to FLAC^{3D} User's Manual. The joint bolts were simulated using beam elements, with both ends of the bolts bounded to corresponding positions on the segment elements.

Figure 7(a) shows a comparison of the vertical displacement curves for S09 and S13 rings between assembled tunnel segments and homogeneous circular pipes, while Fig. 7(b) presents a comparison of the overall displacement curves for the tunnel segments after loading. By taking an example where C-links are set to 18, numerical predictions showed that under incremental loading, the overall displacement results of the tunnel segments matched well with experimental results, verifying the rationality of joint simulation method in this study, which can be used to reflect the stress performance of inter-ring joints. Consistent

results obtained using both shell elements and physical elements also demonstrated that discretizing surface contact into point contact was feasible. Comparing results between uniform and assembled pipes showed that the joint had a significant effect on overall ring stiffness; therefore, inter-segment joints should be considered in long tunnel structural analysis.

C-link numbers relative to B-link numbers also affect results. In Fig. 7(c), load−displacement curve trends of S13 are similar for different numbers of C-links. When C-links are set to 10 or 48, displacement is generally larger or smaller. When C-links are set to 18 and 26 (3 to 4 times the number of B-links), the results are very close, except for a slightly smaller displacement under the final level load. Therefore, to balance computational efficiency and accuracy, it is recommended to set the number of C-links to three times that of B-links for typical tunnel structures, with 16 B-links and 48 C-links in Section 3.

To further validate the applicability of the joint simulation method in practical engineering, the model test results of longitudinal differential settlement of shield tunnels in heterogeneous soft-hard strata in Ref.[37] were verified, where the pipe structure was simulated using ABS plastic pipes with an outer diameter, thickness, and annular width of 0.22 m, 0.01 m, and 0.05 m, respectively. The bolt connections were simplified as springs and also simulated using ABS plastic sheets with a cross-sectional area, length, and quantity of 3×10^{-5} m^2, 0.03 m, and 6, respectively. The elastic modulus and Poisson's ratio of ABS material were 0.2 GPa and 0.3, respectively. The joint model parameters are listed in Set B of Table 2. As shown in Fig. 8, the soil layers beneath the tunnel consist of compacted fly ash layers and free-stacked standard sand layers with K_{30} subgrade coefficients of 44 MPa and 29 MPa, respectively. The soil in the numerical model was modeled using Mohr-Coulomb model. In this study, the subgrade coefficient simulation was used to back-analyze the Mohr-Coulomb parameters for fly ash and standard sand which yielded shear modulus, bulk modulus, friction angle, cohesion values of 33 MPa, 20 MPa, 28º, 4 kPa for fly ash layer, and values of 8.3 MPa, 3.8 MPa, 33º, and 0 kPa for standard sand layer, respectively. The filling above the tunnel was standard sand, and the settlement of the tunnel vaults at different locations is monitored by stepwise surcharge loading on the surface of the soil layer.

It can be seen from Fig. 9 that the overall trend of numerical results is consistent with experimental results. The non-uniform settlement of the tunnel due to differences in soil hardness highlights the applicability of the joint simulation method in this study. The results also demonstrate that non-uniform strata significantly affect structural response and should be carefully considered.

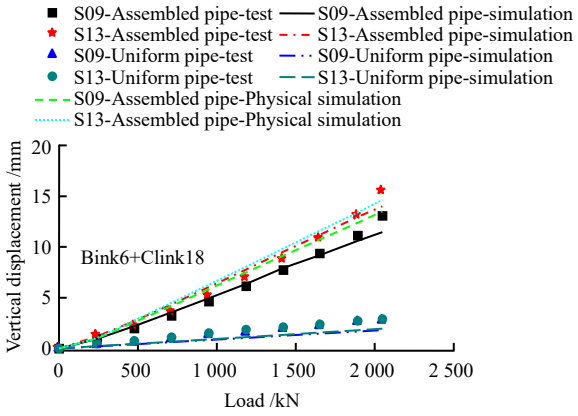

(a) Load displacement curves for S09 and S13 rings of assembled and circular pipes

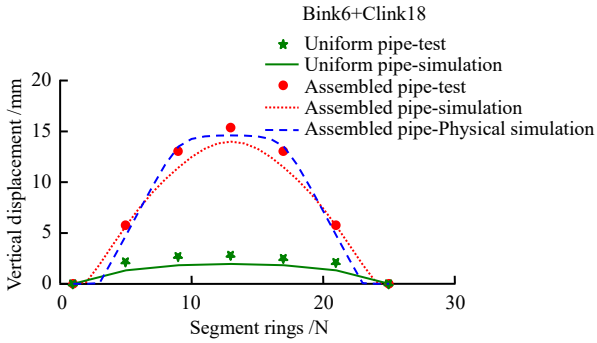

(b) Vertical displacement of whole rings after loading

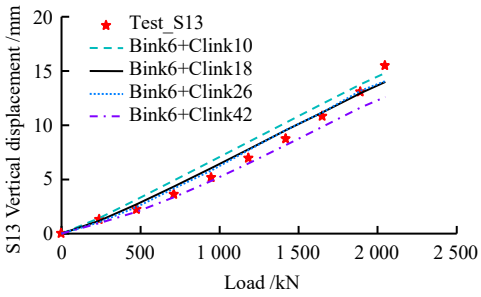

(c) Load-displacement curves of S13 ring with different number of C-links

Fig. 7 Comparisons of vertical displacements at measuring points

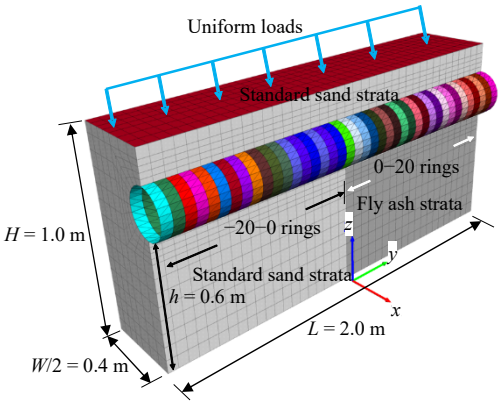

Fig. 8 Diagram of the model test[37]

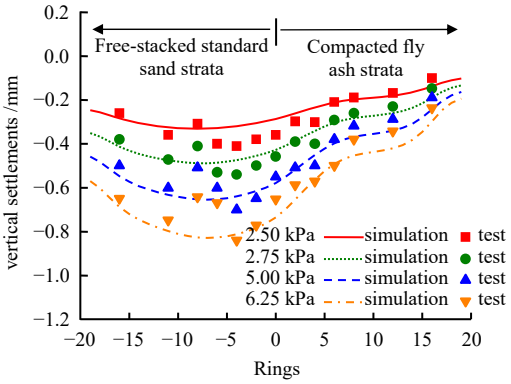

Fig. 9 Comparisons of vertical settlements at measuring points under progressive loading

3 Three-dimensional seismic response analysis of shield tunnels

3.1 Assumptions and simplifications of models

Due to the difficulty in replicating all the details of the actual shield tunnel and hydrogeology in the numerical model, this study makes the following necessary assumptions and simplifications, given its research focus:

(1) The prefabricated concrete segment material is elastic, and local cracking and damage are not considered.

(2) The shield tunnel model only considers inter-ring joints and uses the joint simulation method proposed earlier. The joints inside the ring are not directly considered but are instead reflected through stiffness reduction based on transverse equivalent stiffness theory.

(3) Spatial variability and wave passage effects of seismic motion are not considered. Instead, uniform seismic excitation is applied on the bottom of the model.

(4) Due to grouting effects, the strength of the contact surface between the shield tunnel and saturated sand soil is often high. Therefore, it is assumed that there is a complete connection between shield tunnel segments and surrounding soil elements without considering weakening of contact surface strength.

3.2 Soil and tunnel structural parameters

In this study, the tunnel structural parameters are based on the submarine shield tunnel of Xiamen Rail Transit Line 2, while the geological strata are assumed to be adjacent Toyoura sand strata with different densities. The constitutive model parameters of Toyoura sand are the same as those in Table 1.

The geometric and material parameters of tunnel segments and link bolts are given in Tables 3 and 4[37]. The contacts among rings of the tunnel segments are discretized into 64 link spring connections in the simulation, among which 16 are B-links representing the high-strength bolted connections and the remaining 48 C-links representing the face contact between the ring joints, whose parameters are determined according to the method in Section 2.2. The tangential stiffness of the C-link is selected as the ring joint shear stiffness of 140 MN /m for the tenon occlusion phase given in Ref.[32] (Table 4), which corresponds to a shear stiffness of 122 MN /m, and the stiffness averaged over each C-link in the model is 46.7 MN /m. The specific values are shown in Set C in Table 2.

Table 3 Parameters of the shield tunnel concrete segment

Outer diameter D /m	Thickness t /m	Length l_s /m	Elastic modulus E_c /GPa	Poisson's ratio v
6.7	0.35	1.5	35.5	0.2

Table 4 Parameters of the ring joint bolt

Quantity n	Diameter D /mm	Length l_b /m	Elastic modulus E_b /GPa	Yield tension F_y /MN	Limit tension F_u /MN
16	30	0.4	206	0.452	0.565

3.3 Model building

Figure 10 depicts a three-dimensional model of a shield tunnel passing through adjacent saturated sand layers with varying densities. The coordinate origin is located at the center of the bottom surface, with a model width of 130 m (x-direction), height of 25 m (z-direction), and length of 270 m (y-direction), and the interface is located in the middle of the model. A total of 16 640 shell elements are used to simulate tunnel segments, while 226 200 octahedral solid elements are used to simulate sand layers. In addition, a 2 m-wide low-stiffness elastic material, Duxseal[38], was laid at the left and right sides of the model to reduce boundary effects caused by seismic wave scattering and reflection during dynamic analysis.

Numerical calculation can be divided into two parts: static equilibrium and dynamic analysis. In the stage of initial stress equilibrium, the bottom boundary of the model that has not been excavated is fixed, and the side boundary is constrained in the normal direction. The balance is solved under gravity, and the next step is called "Simultaneous excavation and liner installation". A step-by-step approach is used to balance the fluid and mechanical fields. During the dynamic analysis stage, the normal constraints on the vibrating direction boundary are removed, and a bundled displacement boundary is set on the outside of Duxseal material[20]. The seismic excitation selects the main 20 s acceleration history recorded at Kakogawa station[39] during the 1995 Kobe earthquake. The baseline-corrected time history and spectrum curves are shown in Fig. 11. The scaled acceleration time history is applied to the bottom of the model according to different peak requirements, with vibration direction perpendicular to the longitudinal axis of the tunnel structure. A Rayleigh

damping with a center frequency of 20 Hz and a damping ratio of 0.2% is set for soil elements to reduce noise caused by high-frequency components in calculations. It takes about 3.2 days to complete one calculation example on a computer with a 20-core CPU "Intel Xeon E5-2690 v2 @ 3.00GHz". This paper analyzes parameters such as soil relative density combination, interface inclination angle, and input seismic amplitude. The "Dr8030_03g_dip60" represents a calculation condition where relative densities D_r of layer 1 and layer 2 are 80% and 30%, respectively; interface inclination angle is 60º; and input seismic amplitude is 0.3g.

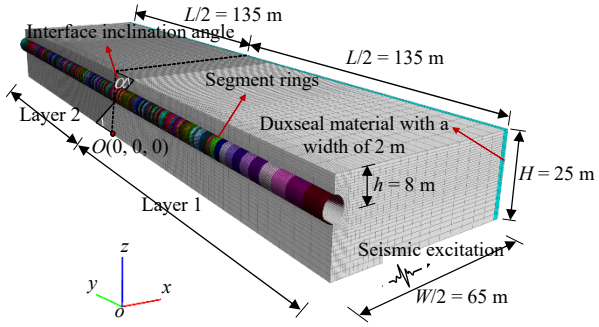

Fig. 10 Layout of the tunnel and soil strata in the numerical model

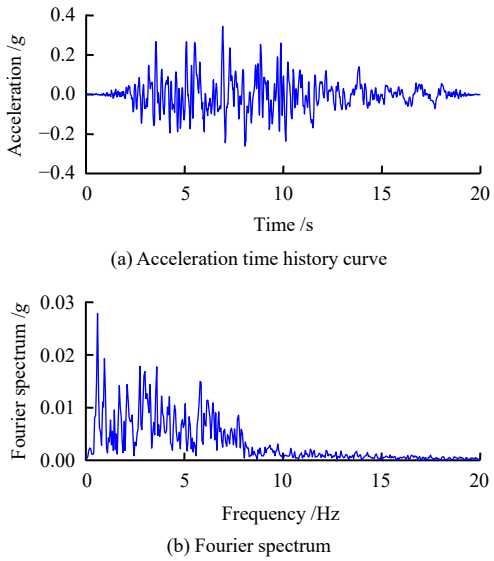

(a) Acceleration time history curve

(b) Fourier spectrum

Fig. 11 Acceleration history and spectrum of Kobe earthquake motion

4 Analysis of numerical results

4.1 Acceleration and pore pressure in strata

As the earthquake progresses, the excess hydrostatic pore water pressure in the soil increases and the effective stress decreases, resulting in a trend of attenuation in acceleration. The liquefaction degree increases as the soil layer relative densities decreases, which is not further elaborated. In present study, the case Dr8030_03g_dip_30/45/90 is taken as an example to examine the effect of interface inclination angle. It should be noted that all results related to different interface inclination angles in the following text are analyzed based on the relative densities combination of 80% and 30% and an input peak acceleration of 0.3g. Figure 12 exhibits the amplification factor β of acceleration at different elevations and positions along different cross-sections in both the tunnel axis (x = 0 m) and away from the tunnel (x = 20 m). The value is generally less than 1 on the loose sand side (y = 20 m/65 m), while slightly greater than 1 on the dense sand side (y = −20 m/ −65 m), with similar patterns for different interface inclination angles. At the interface (y = 0 m) with the inclination angle not equal to 90º, significant amplification of β occurs at elevations close to the tunnel. This may be due to refraction and reflection of vertically propagating shear seismic waves at the interface, resulting in acceleration amplification.

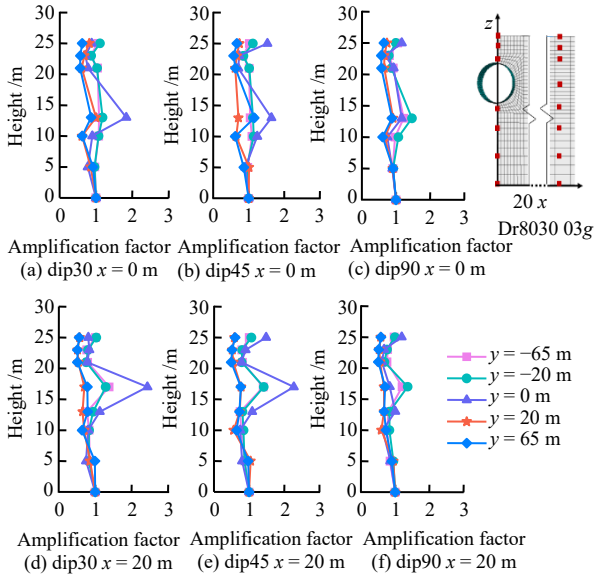

Fig. 12 Acceleration amplification factors measured at different locations in three cases Dr8030_03g_dip_30/45/90

Figure 13 presents the history curves of the excess hydrostatic pore water pressure at monitoring points within cross-sections y = 0 m and y = 30 m under Dr8030_03g_dip90 condition. The patterns of excess hydrostatic pore water pressure are similar in both cross-sections. At monitoring points F1, F2, and F3, which are far from the tunnel (x = 20 m), excess pore pressure increases initially and then gradually stabilizes over time. The presence of the tunnel significantly affects the excess pore pressure around it. The increment of excess pore pressure at monitoring points P1 (arch bottom) and P2 (right side of the tunnel) is remarkably smaller than those at F1 and F2 with the same elevation. Moreover, the excess pore pressure at monitoring point P3 (arch top) shows

an increasing-decreasing trend. This phenomenon is attributed to the uplift of the tunnel structure, which causes surrounding soil to squeeze towards the lower part of the tunnel and pushes the overlying soil of the tunnel towards both sides of tunnel. As a result, significant shear deformation and shear dilation occur, leading to a smaller cumulative value of excess pore pressure, or even negative values at P3. This variation trend in excess pore pressure is similar to that obtained from centrifuge shaking table model tests by Chian et al[40].

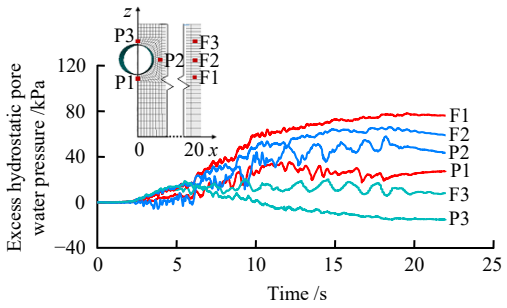

(a) Cross-section 1(y = 0 m)

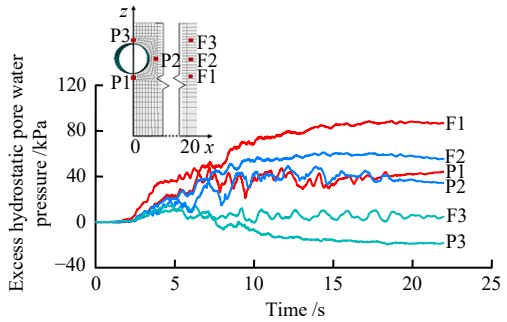

(b) Cross-section 2(y = 30 m)

Fig. 13 Excess pore pressure histories in different sections of the case Dr8030_03*g*_dip90

4.2 Macroscopic deformation patterns of tunnel structures

Under seismic excitation, the tunnel structure experiences different levels of equivalent horizontal seismic inertia forces and vertical uplift forces in saturated sand layers with varying relative densities, resulting in longitudinal variations in deformation. Figure 14 illustrates the deformation mode of the structure at different moments during the earthquake. The tunnel undergoes typical elliptical deformation due to the shear stress from surrounding soil in the cross-section and experiences varying degrees of horizontal deformation and vertical uplift along its axis. Specifically, at the interface between adjacent strata, a sudden change in soil properties leads to significant differences in amplitude and phase of overall deformation along the tunnel. This can be clearly observed from the marked line at the spandrel in Fig. 14, where a twisting deformation mode occurs longitudinally along the tunnel. This mode is also confirmed by analyses of internal forces in section 4.3 and joint displacements in section 4.4.

Figure 15 exhibits variations in maximum uplift at different positions of the vault along the longitudinal direction when the interface inclination angle is 90º. The uplift of tunnels in loose sand is greater than that in dense sand, and it tends to stabilize far away from the interface while undergoing transitional deformation near it. Moreover, peak uplift occurs in the loose sand close to the interface, indicating that interface presence amplifies structural uplift effects more significantly when there are greater differences between adjacent soil relative densities. Figure 16 shows the effect of inclination angle on uplift. When far from an interface, uplift is generally consistent regardless of inclination angle; however, near the interface with a larger angle, overall uplift increases because a larger angle implies larger liquefiable soil volumes beneath tunnels that lead to greater structural uplift under seismic loads. In other words, when inclination angle is vertical (i.e., 90º), it represents a worst-case scenario for structural uplift.

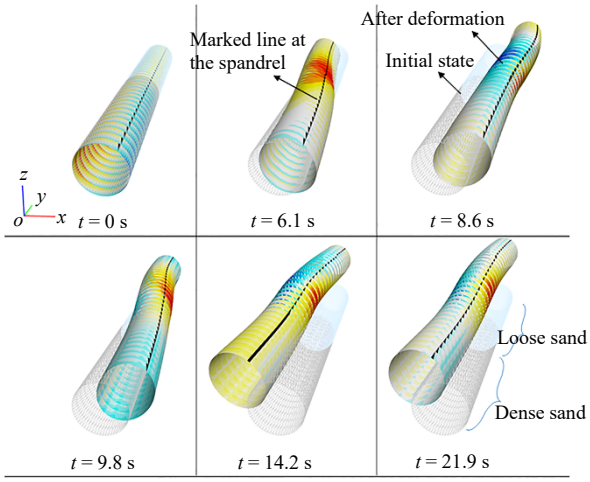

Fig. 14 Tunnel deformation modes at various moments (enlarged 20 times)

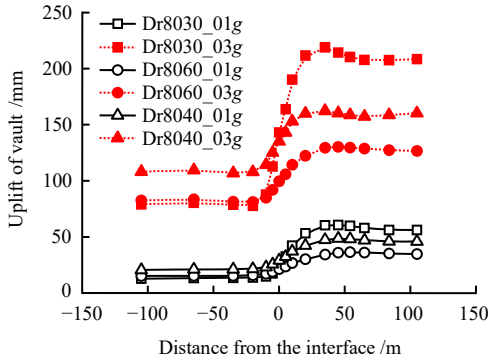

Fig. 15 Uplifts of tunnel along the longitudinal direction in various calculating cases with 90-degree dip angle

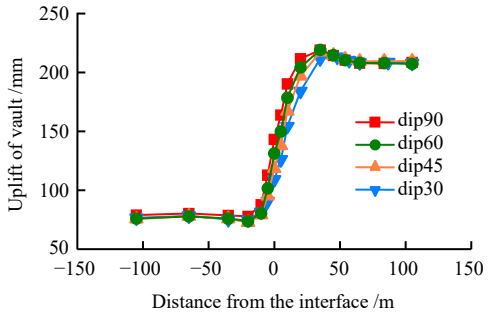

Fig. 16 Uplifts of tunnel along the longitudinal direction at four cases: Dr8030_03*g*_dip_30/45/60/90

4.3 Displacement of segments

The normal compressive and tangential displacement peaks of the C-link representing face-contacts of concrete are 0.143 mm and 3.55 mm, respectively. Since the compression along the normal direction is minimal and more attention is paid to whether the bolts are sheared along the tangential axis, this paper focuses on analyzing the B-link representing bolt connections. The peak shear and tensile displacements under various working conditions increase with increasing input acceleration peaks. When there is a greater difference in relative density between adjacent soil layers, the displacement of joint bolts is greater. The maximum tensile and shear displacements of the B-link under all working conditions are 0.547 mm and 3.59 mm, respectively, corresponding to maximum tensile stress and shear stress of 281.6 MPa and 308.1 MPa, respectively. The yield stresses along the normal and tangential directions of this type of bolt are 640 MPa and 448 MPa, respectively, both greater than their calculated values. In other words, neither normal nor tangential bolts have yielded during dynamic calculations.

Based on this, further research is conducted on the location where maximum displacement occurs in joints and how the interface inclination angle affects joint displacement. Figure 17 plots the peak tensile displacements at six monitoring points within a cross-section under Dr8030_03*g*_dip90 working conditions. Monitoring points at vault (90º) and bottom (270º) are taken as examples for analysis, it can be seen that peak tensile displacement occurs in loose sand at vault while it is very small in dense sand; however, it is opposite at the bottom. This indicates that the tunnel structure experiences tension at the bottom in the dense sand side of the transition zone, while at the loose sand side, tension occurs at the vault, consistent with the overall uplift pattern of the tunnel. Similarly, monitoring points at 45º and 225º also follow a similar pattern, which further confirms that the deformation of tunnel structure in loose sand and dense sand under seismic action is not consistent, with a certain phase difference. Figure 18 shows the maximum radial and circumferential shear displacement curves of diagonal axis at each cross-section under Dr8030_03*g*_dip90 working conditions. Both curves have similar patterns, with the maximum shear displacement occurring near the interface. Moreover, there is significant shear displacement in the joint near loose sand side of the interface, with a second peak value appearing. Obviously, the greater the shear displacement of the joint, the greater the overall deformation of the structure, which is consistent with the law described in Fig. 15 that shows greater uplift on loose sand side at interface and near it.

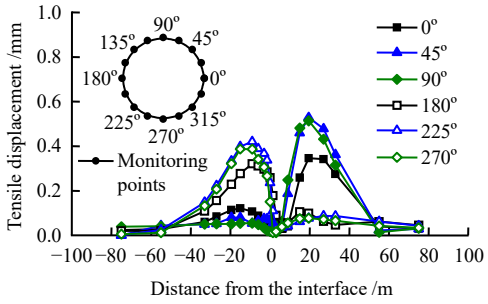

Fig. 17 Maximum tensile displacements at monitoring points of the section along the longitudinal direction in the case Dr8030_03*g*_dip_90

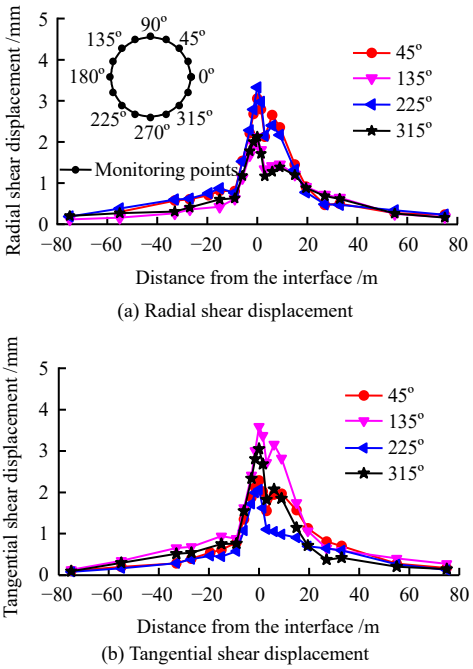

Fig. 18 Maximum radial and tangential shear displacements at monitoring points of the section along the longitudinal direction in case Dr8030_03*g*_dip_90

The inclination angle of the soil layer interface also affects the joint displacement. The distribution of joint displacement peaks at different interface inclination angles is potted in Fig. 19. The shear displacement of the joint shows a trend of increasing first and then decreasing along the vertical direction, peaking near the loose sand adjacent to the interface. When the interface inclination angle is

larger, the displacement on the loose sand side is larger, and the second peak is more obvious. This is consistent with the law described in Fig. 16. The tensile displacement of joint bolts shows a clear bimodal pattern, and it is small near the loose sand adjacent to the interface. The interface inclination angle has a significant effect on tensile deformation in tunnel sections located in loose sand. It can be seen that joint shear displacement increases with increasing interface inclination angle.

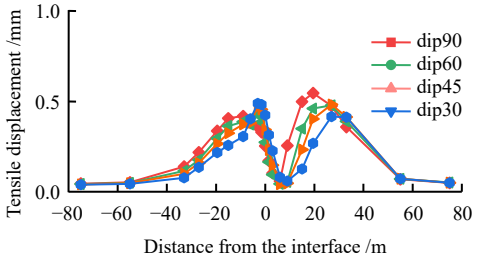

(a) Tensile displacement

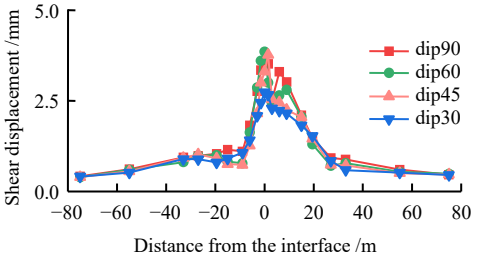

(b) Shear displacement

Fig. 19 Maximum tensile and shear displacements of connecting bolts along the longitudinal direction in four cases: Dr8030_03*g*_dip_30/45/60/90

The above rules for joint displacement indicate that shear displacement is dominant at segment joints near loose sand adjacent to the interface, while there are additional displacement peaks on the loose sand side for tensile displacement except at interfaces. This should be taken into account in designing bolt joints for shield tunneling, although further exploration is needed to determine their specific location and range of peak displacements.

4.4 Internal forces of the tunnel segment

The longitudinal deformation of tunnel structures varies in magnitude and phase, which inevitably leads to differences in their internal force response along the longitudinal direction. We take the in-plane bending moment as an example, Fig. 20 shows the dynamic bending moment history at the 45º position of the spandrel under the Dr8030_03*g*_dip90 condition. As the earthquake progresses, there are significant differences in both the magnitude and phase of the bending moment, with a lag effect on the dense sand side (y = −55 m) compared to the loose sand side (y = 55 m). Based on this, further research was conducted on the influence of interface inclination angle on bending moment. Figure 21 shows the distribution of bending moments at various positions within the tunnel section, which exhibits a typical butterfly-shaped distribution corresponding to an elliptical deformation mode within the tunnel section, indicating that maximum response occurs at diagonal positions. Similar patterns were observed for different interface inclination angles, with peak bending moment occurring at an angle of 30º.

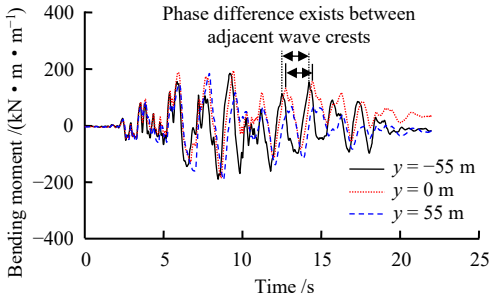

Fig. 20 Bending moment histories of the tunnel along the longitudinal direction in the case Dr8030_03*g*_dip_90

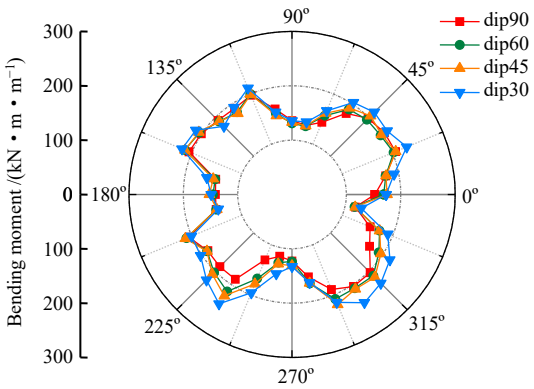

Fig. 21 Distribution of bending moments of segments on the soil interface in four cases: Dr8030_03*g*_dip_30/45/60/90

Figure 22 illustrates the distribution of peak dynamic bending moment, axial force, and shear force of each segment of the tunnel along the longitudinal axis. It can be observed that there is a sudden change in internal forces at the interface where the maximum shear force occurs. The axial force exhibits a M variation trend, consistent with the deformation characteristics of joint shear and tensile displacement discussed in section 4.3. Additionally, as the inclination angle increases, the axial force gradually increases, consistent with the trend of greater uplift with larger angles. The bending moment pattern exhibits a Z variation trend near the interface, with larger peak values for greater inclination angles. The peak bending moment occurs on the dense sand side near the interface and decreases on the loose sand side due to phase differences in tunnel deformation between different densities. Owing to weaker constraint effect, loose sand serves as a transitional zone for deformation, resulting in bending moment equilibrium.

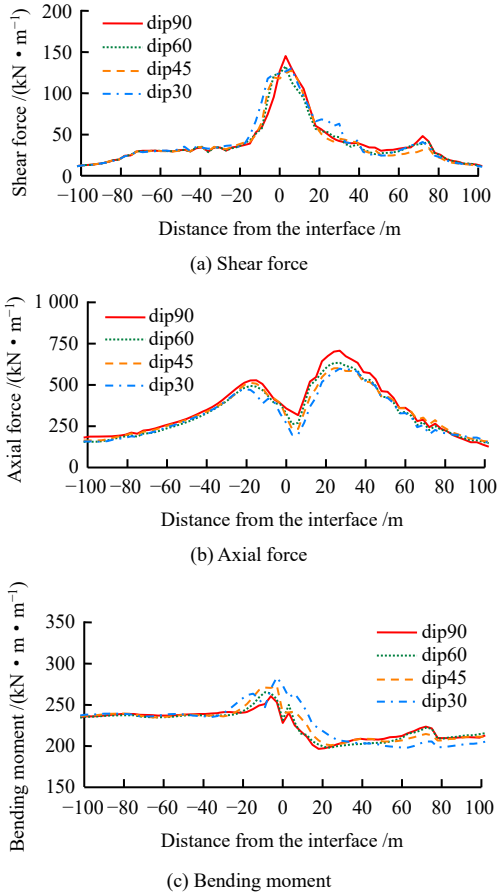

Fig. 22 Maximum moment, axial force and shear force of each cross-section along the longitudinal direction in four cases: Dr8030_03*g*_dip_30/45/60/90

5 Conclusions

Tunnel sections located at the boundaries of different liquefaction resistance strata are more susceptible to severe earthquake damage, yet there is a lack of research in the literature on this seismic response pattern. This paper conducts an in-depth three-dimensional numerical analysis study, after verifying the rationality of the adopted numerical simulation method, to reveal the seismic response patterns of shield tunnels passing through saturated sand layers with different densities. The main conclusions are listed as follows:

(1) The seismic response of tunnels varies significantly in soil layers with different densities, especially at the interfaces between different geological layers as well as in loose sand near the interface. The interface inclination angle affects the response of the segment near the interface. The greater the inclination angle, the greater the uplift of the segment. The vertical inclination angle is the most unfavorable situation.

(2) The maximum shear displacement of joint bolts occurs near the interface, and the maximum tensile displacement exhibits a bimodal pattern along the longitudinal direction, appearing respectively at the dense sand adjacent to the interface and in the loose sand. The form of joint bolts and seismic design in these positions should be given special consideration.

(3) Due to different soil constraints, tunnels exhibit differences in both vertical and horizontal deformation amplitude and phase. Inconsistencies in structures deformation near interface cause tunnel deformation to occur in a twisting pattern similar to that of a corkscrew. Special attention should be paid to this phenomenon in seismic design for shield tunnels.

References

[1] DU Xiu-li, LI Yang, XU Cheng-shun, et al. Review on damage causes and disaster mechanism of Daikai subway station during 1995 Osaka-Kobe Earthquake[J]. Chinese Journal of Geotechnical Engineering, 2018, 40(2): 223−236.

[2] DATTA T K. Seismic response of buried pipelines: a state-of-the-art review[J]. Nuclear Engineering and Design, 1999, 192(2): 271−284.

[3] WANG T, KWOK O A, JENG F. Seismic response of tunnels revealed in two decades following the 1999 Chi-Chi earthquake (Mw 7.6) in Taiwan: a review[J]. Engineering Geology, 2021, 287: 106090.

[4] LIANG Jian-wen. Dynamic analysis of pipelines laid through three-soil media[J]. Journal of Tianjin University, 1998, 31(2): 36−41.

[5] YU H, ZHANG Z, CHEN J, et al. Analytical solution for longitudinal seismic response of tunnel liners with sharp stiffness transition[J]. Tunnelling and Underground Space Technology, 2018, 77: 103−114.

[6] ZOU Yan, JING Li-ping, LI Yong-qiang. Study of shaking table model test of tunnel through soil interface[J]. Chinese Journal of Rock Mechanics and Engineering, 2014, 33(Suppl.1): 3340−3348.

[7] ZHANG Jing, HE Chuan, GENG Ping, et al. Shaking table tests on longitudinal seismic response of shield tunnel through soft-hard stratum junction[J]. Chinese Journal of Rock Mechanics and Engineering, 2017, 36(1): 68−77.

[8] WANG D, YUAN J, CUI G, et al. Experimental study on characteristics of seismic damage and damping technology of absorbing joint of tunnel crossing interface of soft and hard rock[J]. Shock and Vibration, 2020, 2020(1): 1−13.

[9] LIANG J, XU A, BA Z, et al. Shaking table test and numerical simulation on ultra-large diameter shield tunnel passing through soft-hard stratum[J]. Soil Dynamics and Earthquake Engineering, 2021, 147: 106790.

[10] DARLI C M, AIPING T, DELONG H, et al. Large scale shaking table model test and analysis on seismic response of utility tunnel in non-homogeneous soil[J]. Earthquake Engineering and Engineering Vibration, 2021, 20(2): 505−515.

[11] LIU Guang-lei, SONG Er-xiang, LIU Hua-bei. Numerical modeling of subway tunnels in liquefiable soil under earthquakes and verification by centrifuge tests[J]. Chinese

Journal of Geotechnical Engineering, 2007, 29(12): 1815−1822.

[12] CHIAN S C, TOKIMATSU K, MADABHUSHI S P G. Soil liquefaction-induced uplift of underground structures: physical and numerical modeling[J]. Journal of Geotechnical and Geoenvironmental Engineering, 2014, 140(10): 04014057.

[13] ZHUANG Hai-yang, FU Ji-sai, CHEN Su, et al. Liquefaction and deformation of the soil foundation around a subway underground structure with a slight inclined ground surface by the shaking table test[J]. Rock and Soil Mechanics, 2019, 40(4): 1263−1272.

[14] ZHENG Gang, YANG Peng-bo, ZHOU Hai-zuo, et al. The uplift response of rectangular tunnel in liquefiable soil[J]. China Civil Engineering Journal, 2019, 52(Suppl.1): 257−264.

[15] LIU Hua-bei, SONG Er-xiang. Earthquake induced liquefaction response of subway structure in liquefiable soil[J]. Rock and Soil Mechanics, 2005, 26(3): 381−386, 391.

[16] DAFALIAS Y F, MANZARI M T. Simple plasticity sand model accounting for fabric change effects[J]. Journal of Engineering Mechanics, 2004, 130(6): 622−634.

[17] BOULANGER R W, ZIOTOPOULOU K. Formulation of a sand plasticity plane-strain model for earthquake engineering applications[J]. Soil Dynamics and Earthquake Engineering, 2013, 53: 254−267.

[18] WANG Rui. Single piles in liquefiable ground: seismic response and numerical analysis methods[D]. Beijing: Tsinghua University, 2014.

[19] CHENG Z, DETOURNAY C. Formulation, validation and application of a practice-oriented two-surface plasticity sand model[J]. Computers and Geotechnics, 2021, 132: 103984.

[20] CHEN Ren-ren. Underground structures in liquafiable ground: seismic response and numerical analysis method[D]. Beijing: Tsinghua University, 2018.

[21] WANG R, ZHANG J, WANG G. A unified plasticity model for large post-liquefaction shear deformation of sand[J]. Computers and Geotechnics, 2014, 59: 54−66.

[22] YE Z, LIU H. Mechanism and countermeasure of segmental lining damage induced by large water inflow from excavation face in shield tunneling[J]. International Journal of Geomechanics, 2018, 18(12): 4018161−4018163.

[23] CHEN G X, RUAN B, ZHAO K, et al. Nonlinear response characteristics of undersea shield tunnel subjected to strong earthquake motions[J]. Journal of Earthquake Engineering, 2020, 24(3): 351−380.

[24] MIAO Yu, CHEN Chao, RUAN Bin, et al. Crossing river shield tunnel longitudinal seismic response analysis based on generalized displacement method[J]. Journal of Beijing University of Technology, 2018, 44(3): 344−350.

[25] LIAO Shao-ming, HOU Xue-yuan, PENG Fang-le. Longitudinal shear transfer of tunnel and its 1D analytical solution[J]. Chinese Journal of Rock Mechanics and Engineering, 2005, 24(7): 1110−1116.

[26] WU H, SHEN S, LIAO S, et al. Longitudinal structural modelling of shield tunnels considering shearing dislocation between segmental rings[J]. Tunnelling and Underground Space Technology, 2015, 50: 317−323.

[27] DO N A, DIAS D, ORESTE P. Simplified approach to the design of segmental tunnel linings[J]. Proceedings of the Institution of Civil Engineers-Geotechnical Engineering, 2018, 171(3): 209−214.

[28] DO N, DIAS D, ORESTE P. 3D numerical investigation of mechanized twin tunnels in soft ground – Influence of lagging distance between two tunnel faces[J]. Engineering Structures, 2016, 109: 117−125.

[29] ITASCA C G. Fast Lagrangian analysis of continua in three dimensions[M]. Minnesota: [s. n.], 2019.

[30] EL-SEKELLY W, DOBRY R, ABDOUN T, et al. Evaluation of field sand liquefaction including partial drainage under low and high overburden using a generalized bounding surface model[J]. Soil Dynamics and Earthquake Engineering, 2022, 152: 107059.

[31] KOSEKI J, MATSUO O, KOGA Y. Uplift behavior of underground structures caused by liquefaction of surrounding soil during earthquake[J]. Soils and Foundations, 1997, 37(1): 97−108.

[32] SANG Yun-long, LIU Xue-zeng, ZHANG Qiang. Stiffness analysis and application of segment annular joint based on bolt-concave and convex tenon connection in metro shield tunnel[J]. Tunnel Construction, 2020, 40(1): 19−27.

[33] YAN Zhi-guo, PENG Yi-chen, DING Wen-qi, et al. Load tests on segment joints of single lining structure of shield tunnel in Qingcaosha Water Conveyance Project[J]. Chinese Journal of Geotechnical Engineering, 2011, 33(9): 1385−1390.

[34] ZHU He-hua, HUANG Bo-qi, LI Xiao-jun, et al. Unified model for internal force and deformation of shield segment joints and experimental analysis[J]. Chinese Journal of Geotechnical Engineering, 2014, 36(12): 2153−2160.

[35] YE Fei, YANG Peng-bo, MAO Jia-ye, et al. Longitudinal rigidity of shield tunnels based on model tests[J]. Chinese Journal of Geotechnical Engineering, 2015, 37(1): 83−90.

[36] SEDARAT H, KOZAK A, HASHASH YMA, et al. Contact interface in seismic analysis of circular tunnels[J]. Tunnelling and Underground Space Technology, 2009, 24(4): 482−490.

[37] CHEN Xiao-jian. Similar model test study of longitudinal differential settlement of shield tunnel in soft-hard uneven strata[J]. Tunnel Conscruction, 2019, 39(Suppl.1): 57−64.

[38] GAO M, TIAN S P, HE R, et al. Numerical analysis on the ground vibration isolation of duxseal[J]. Advances in Civil Engineering, 2019(4): 1−10.

[39] PEER. Pacific earthquake engineering research center. Ground Motion Database[CP]. [2022-05-18]. https://ngawest2.berkeley.edu.

[40] CHIAN S C, MADABHUSHI S P G. Excess pore pressures around underground structures following earthquake induced liquefaction[J]. International Journal of Geotechnical Earthquake Engineering, 2012, 3(2): 25−41.